Research Article

3D Surface Analysis of Hippocampal Microvasculature in the Irradiated Brain

Brianna M. Craver,[1] Munjal M. Acharya,[1] Barrett D. Allen,[1] Sarah N. Benke,[1] Nan W. Hultgren,[2] Janet E. Baulch,[1] and Charles L. Limoli[1]*

[1]*Department of Radiation Oncology, University of California, Irvine, California 92697-2695*

[2]*Department of Molecular Biology and Biochemistry, University of California, Irvine, California 92697*

Cranial irradiation used to control CNS malignancies can also disrupt the vasculature and impair neurotransmission and cognition. Here we describe two distinct methodologies for quantifying early and late radiation injury in CNS microvasculature. Intravascular fluorescently labeled lectin was used to visualize microvessels in the brain of the irradiated mouse 2 days post exposure and RECA-1 immunostaining was similarly used to visualize microvessels in the brain of the irradiated rat 1-month post exposure. Confocal microscopy, image deconvolution and 3-dimensional rendering methods were used to define vascular structure in a $\sim 4 \times 10^7$ μm^3 defined region of the brain. Quantitative analysis of these 3D images revealed that irradiation caused significant short- and long-term reductions in capillary density, diameter and volume. In mice, irradiation reduced mean vessel volume from 2,250 to 1,470 μm^3 and mean vessel diameter from 5.0 to 4.5 μm, resulting in significant reductions of 34% and 10%, in the hippocampus respectively. The number of vessel branch points and area was also found to also drop significantly in mice 2 days after irradiation. For rats, immunostaining revealed a significant, three-fold drop in capillary density 1 month after exposure compared to controls. Such radiation-induced disruption of the CNS microvasculature may be contributory if not causal to any number of neurocognitive side effects that manifest in cancer patients following cranial radiotherapy. This study demonstrates the utility of two distinct methodologies for quantifying these important adverse effects of radiotherapy. Environ. Mol. Mutagen. 00:000–000, 2016. © 2016 Wiley Periodicals, Inc.

Key words: irradiation; microvasculature; hippocampus

INTRODUCTION

Cranial irradiation remains the frontline treatment for CNS malignancies, providing the best available restraint on disease progression. While targeted radiotherapy has enhanced tumor cell kill, normal tissue damage is an unavoidable consequence of such procedures that can lead to an array of unintended side effects [Tofilon and Fike, 2000; Fike et al., 2009]. Neurocognitive complications are typically associated with the radiotherapeutic management of brain cancer and can be caused by a number of underlying pathologies [Abayomi, 1996; Meyers, 2000; Surma-aho et al., 2001]. Past work from our laboratory and those of others has found cranial radiation exposure to be linked to the inhibition of neurogenesis [Mizumatsu et al., 2003; Parihar et al., 2014], reduction of dendritic complexity [Parihar and Limoli, 2013; Parihar et al., 2015] and increased neuroinflammation [Parihar et al., 2014; Acharya et al., 2015b]. The study of radiation injury to the brain has a long history, and has been reviewed by several groups over the last 15 years [Tofilon and Fike, 2000; Wong and Van der Kogel, 2004; Greene-Schloesser et al., 2012]. Past controversy regarding the critical target cells (parenchymal oligodendrocytes or stromal endothelial cells) for normal tissue injury that can be dose limiting in

Additional Supporting Information may be found in the online version of this article.

Grant sponsor: HDTRA; Grant number: 1-13-1-0022; Grant sponsor: NINDS; Grant number: R01NS089575; Grant sponsor: NINDS; 2R01NS074388-05.

*Correspondence to: Prof. Charles L. Limoli, Department of Radiation Oncology, University of California Irvine, Medical Sciences I, Room B-146B, Irvine, CA 92697-2695, USA. E-mail: climoli@uci.edu

Received 6 November 2015; provisionally accepted 24 March 2016; and in final form 00 Month 2016

DOI 10.1002/em.22015

Published online 00 Month 2016 in Wiley Online Library (wileyonlinelibrary.com).

the clinical setting [van der Kogel, 1986], has subsided in light of new data. Current views of radiation injury incorporate the concept of secondary reactive processes in which temporally complex waves of oxidative stress and inflammation conspire to disrupt CNS function at many levels [McBride, 1995; Tofilon and Fike, 2000; Wong and Van der Kogel, 2004; Fike et al., 2009]. One target of these processes is the microvasculature. For many years it has been acknowledged that irradiation could compromise vascular structure [Reinhold et al., 1990] and lead to dose-dependent endothelial apoptosis [Ljubimova et al., 1991; Pena et al., 2000; Li et al., 2003]. Based on a wealth of past data, it seems likely that certain negative neurocognitive consequences of cranial irradiation may be linked to disruptions of the microvasculature network.

Recent advances in imaging techniques have provided unprecedented capability to quantify radiation-induced changes to neuronal structure [Parihar and Limoli, 2013; Parihar et al., 2015] and microvasculature [Robertson et al., 2015]. State-of-the-art software algorithms now enhance the ability to quantify structural changes to critical CNS structures, and evaluate the effects of irradiation on the microvasculature using a variety of novel techniques. Here we demonstrate how the use of the Imaris software platform can expedite the imaging and analysis of the microvasculature, which can be paired with previously described techniques to quantify these changes in the irradiated brain.

MATERIALS AND METHODS

Animals and Irradiation

All animal procedures were carried out in accordance with NIH and Institutional Animal Care and Use Committee guideline using 8-month-old male mice (C57Bl6/J, Jackson) and 6-month-old athymic nude rats (ATN, Cr:NIH-Foxn1rnu, strain 316, Charles River), $N = 4$–6 per group. For irradiation, animals were anesthetized using isoflurane (5% induction, 2.5% maintenance) and placed ventrally on a treatment table (XRAD 320 irradiator, Precision X-ray) without restraint. The head was positioned using a 1.0 cm^2 diameter collimator to shield the cerebellum, eyes and rest of the body from radiation exposure. A beam-conditioning filter was used to filter out low energy X-rays and minimize skin damage (0.75 mm Sn + 0.25 mm Cu + 1.5 mm Al; HVL = 3.7 mm Cu, half value layer). Mice were subjected to 9 Gy head-only irradiation and rats were subjected to 10 Gy head-only irradiation, delivered at a dose rate of 1.0 Gy min^{-1}. Mice were euthanized 2 days after irradiation and 30 min after injection of lectin, rats were euthanized 30 days after irradiation.

Lectin Injections and Perfusions

To visualize the blood vessels in the brain, Dylight 488 or 594-labeled *Lycopersicon esculentum* tomato lectin (Vector Laboratories, Burlingame) was administered via tail vein injection. Mice were anesthetized with isofluorane and 1 ml saline was injected subcutaneously. Fur was removed from the tail (Veet; Reckiff Benckisen, Parsippany, NJ) and body temperature was maintained at 37°C using a heating pad. An insulin syringe was used to inject 100 μl of lectin per animal in the tail vein (BD Insulin Syringes with Ultra-Fine needle, 31G). After 30 min, animals were sacrificed and perfused with 4% paraformaldehyde (Acros Organics, Geel, Belgium, http://www.acros.com). Brain tissues were subsequently processed for coronal sectioning (30-μm thick using a cryostat; Leica Microsystems, Wetzlar, Germany, http://www.leica.com).

Immunostaining

Serial sections through the middle of the hippocampus were selected for staining and washed in Tris-buffered saline (TBS; 100 mM, pH 7.4; Sigma–Aldrich, St. Louis, MO, http://www.sigmaaldrich.com). For RECA-1 immunostaining, free-floating sections were incubated in 30% H_2O_2 for 30 min followed by Tris-A for 20 min (TBS with 0.1% Triton-X-100; Sigma–Aldrich). Sections were blocked with 10% normal donkey serum and incubated in mouse anti-RECA-1 antibody overnight (1:200, AbD Serotec). Sections were incubated for 1 hr with biotinylated donkey anti-mouse (1:200) secondary antibody and color was developed using the ABC Elite and Vector SG kits (Vector Labs, USA). Sections were counterstained using nuclear fast red. For lectin injected mouse tissues, sections were counterstained using DAPI (1 mmol l^{-1} in TBS for 15 min; Life Technologies, Invitrogen) to visualize cells and mounted in ProLong Diamond Antifade Mountant (Refractive index: 1.47; ref. P36970; Life Technologies, Eugene, OR).

Image Acquisition

Images were acquired using a laser-scanning confocal microscope (Nikon Eclipse Ti, EZ-C1 interface, Japan) with NIS-Elements AR software (version 4.30.02; Nikon) equipped with a 20×/0.75 NA objective (Nikon). Approximately 30 z-stack images at 1-μm were obtained to analyze blood vessels. Fluorescent Dylight 488 lectin was imaged with 493 nm excitation and 518 nm emission and Dylight 594 lectin was imaged with 592 nm excitation and 617 nm emission.

3D Quantification of Microvasculature

Images were deconvoluted using AutoQuant software (version X3.0.4, 64-Bit Edition; Media Cybernetics, Rockville, MD). Spacing was set to 1.26867 × 1.26867 × 1 (μm); and wavelengths were set at 447 nm (DAPI) and 785 nm (TRITC). An adaptive, theoretical PSF (blind) deconvolution method was used. Deconvoluted images were imported into Imaris x64 (version 8.1.2, Bitplane AG, Zurich, Switzerland) for 3D surface rendering and quantitative analysis of vessel parameters. After display adjustment, the DAPI filter was removed to view the images in Blend mode with rendering quality set to 100%. Background subtraction was set to 9.25 μm and the threshold was reduced in order for surfaces to fully cover all vessels. A volume filter was applied to remove nonspecific staining and minimum thresholds were used for both unirradiated and irradiated groups. To quantify vessel length and branch points, a "Filament Trace" was created from a masked surface channel using a threshold (loops) algorithm setting. A minimal ratio of branch length to trunk radius was set to 6. The same threshold parameters were used for both control and irradiated groups.

RECA-1 + Microvessel Tracing

Stereological assessment was conducted using a Nikon microscope (Nikon TE2000-E, Japan) equipped with a MBF color digital camera, 20×/0.75 NA objective lens (Nikon), 3-axis motorized stage (Bio Precision 2, Ludl, NY), and Neurolucida (StereoInvestigator, MBF Bioscience, VT). Systemic random sampling (SRS) and image stack analysis modules were used to acquire batch images through the anterior-posterior planes of the hippocampus. The acquired images were

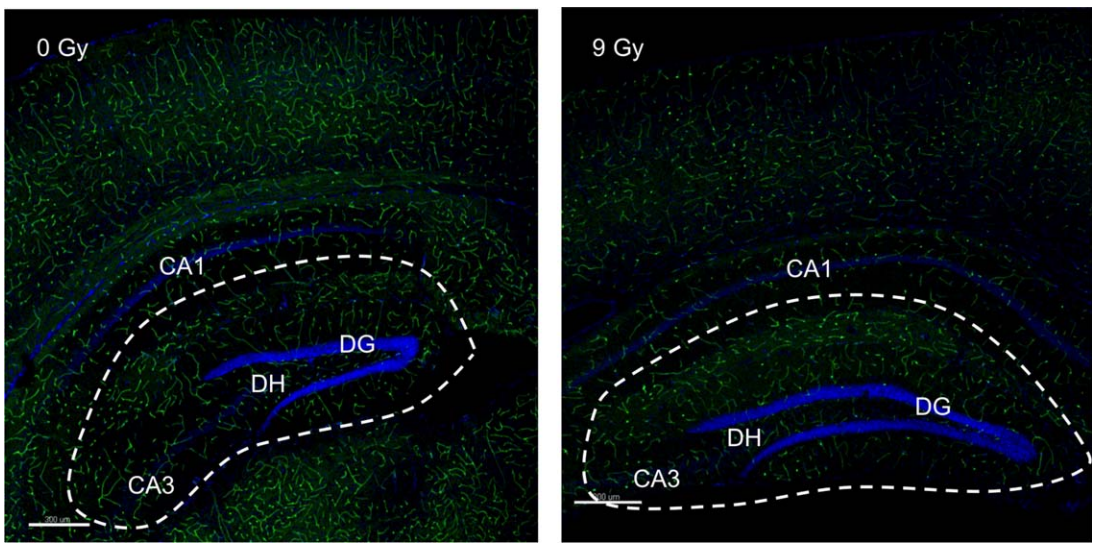

Fig. 1. Hippocampus of unirradiated and irradiated mice injected with Tomato Lectin 488. Dashed line delineates the Dentate Gyrus (DG) region that was analyzed for quantification of microvessel parameters. Images were taken at 4×/0.2 NA. Scale bar = 300 μm.

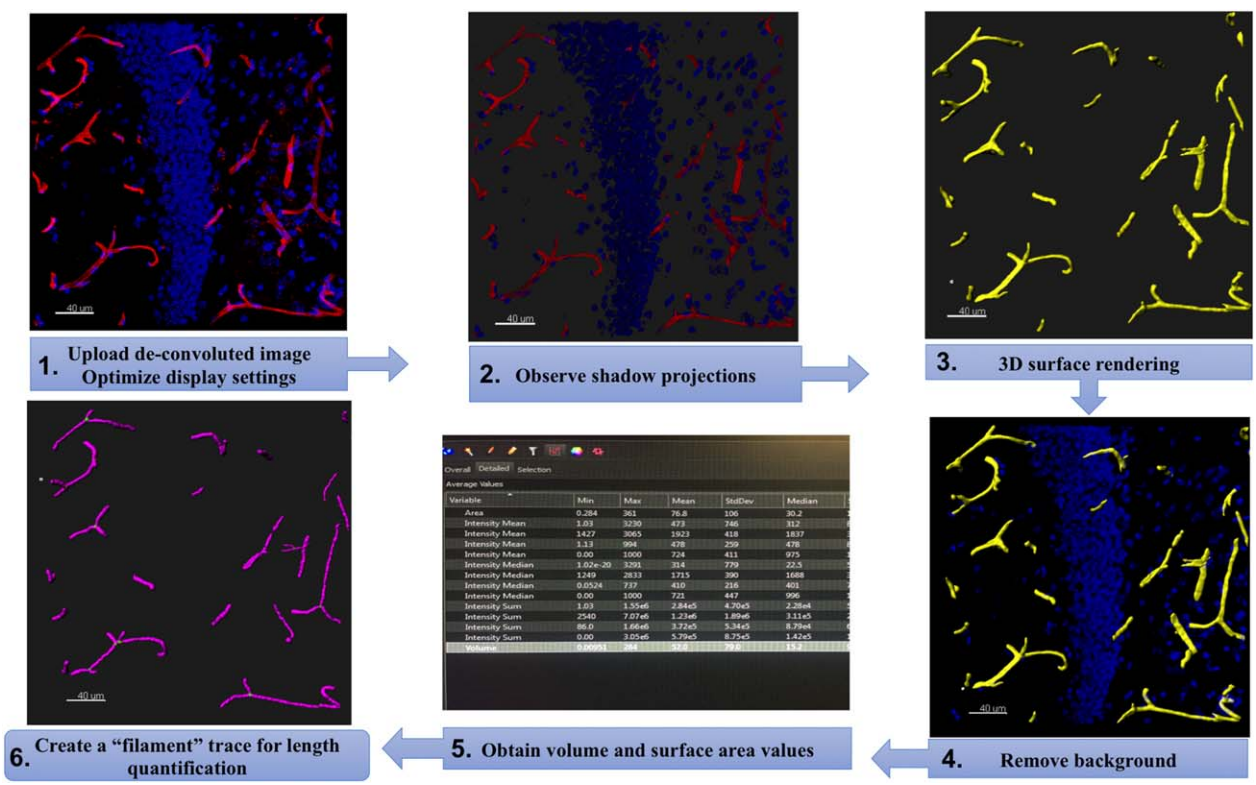

Fig. 2. Work flow of microvessel analysis. Display settings were optimized for control images and maintained throughout experiment. The 3D surface rendering provides quantitative analyses including total vessel number, volume, and surface area. Filament trace provides quantification of vessel length and number of branch points.

uploaded on an MBF Workstation (MBF Biosciences) and the RECA-1+ positive vessels (black, on a nuclear fast red counterstained background) were traced for volumetric quantification using Neurolucida tracing and SRS according to unbiased stereological principles. All analyses were conducted blind from coded slides (9–12 hippocampus/animal, $n = 4$–6 animals/group).

Statistical Analysis

All statistical analyses were performed using GraphPad Prism software (version 6.0, La Jolla, CA) where data were assessed for significance at a level of $P < 0.05$ by two-tailed Student's T tests. All data were represented as mean ± standard error of the mean (SEM).

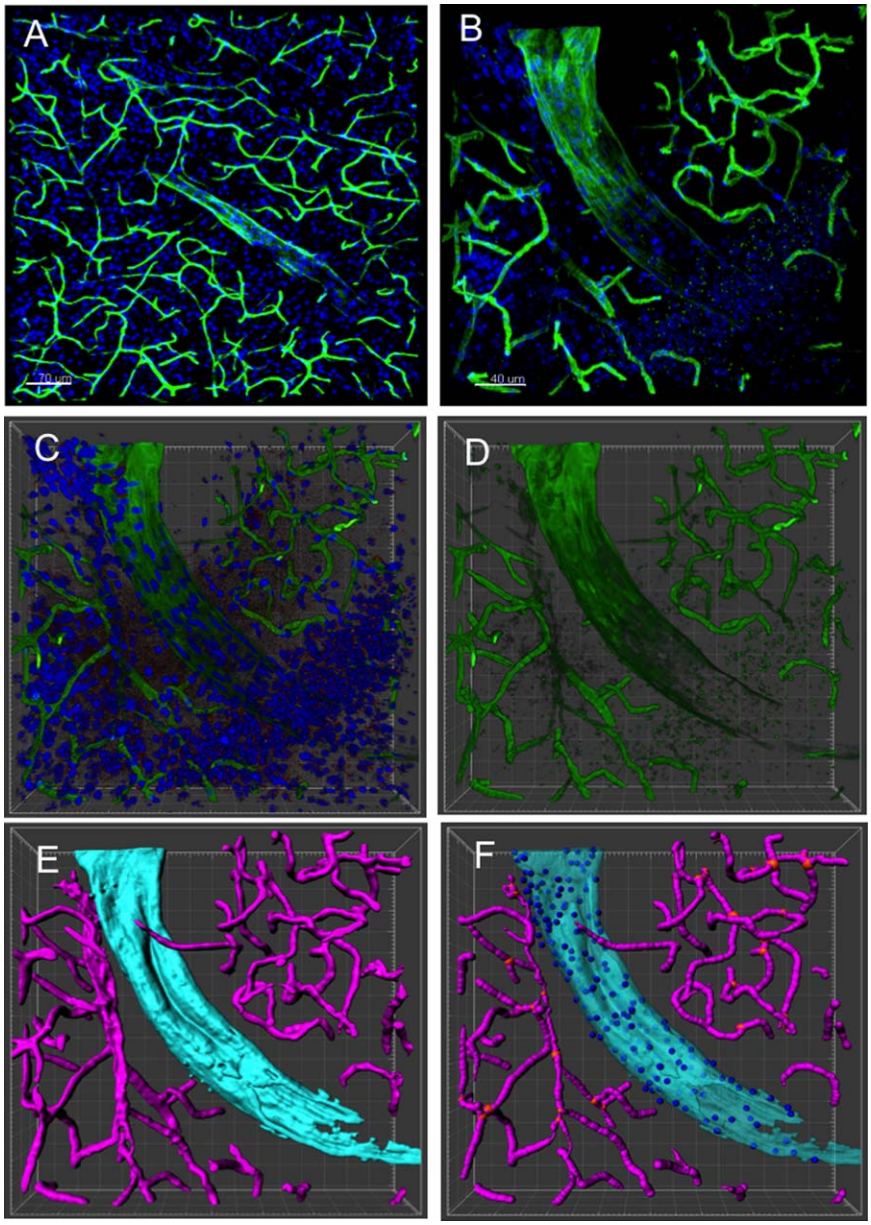

Fig. 3. Tomato lectin allows for rapid identification and 3D surface rendering of blood vessels throughout the brain. (**A**,**B**) Lectin 488 (green) was administered to mice via tail vein injection and animals were perfused 30 minutes later. Brains were sectioned and stained with DAPI counterstain (blue) to identify nuclei (20×/0.75 NA). Scale bars 70 and 40 μm, respectively. (**C**–**F**) 3D surfaces created using Imaris software allows for detailed analysis of microvessels based on volume, area, or length. (**C**) Nuclei were identified using DAPI counterstain (blue). Images are evaluated using the "Blend" setting to observe vessels and nuclei in 3D. (**D**) Background nuclei were then removed by turning the DAPI channel off for vessel analysis. (**E**) After 3D surface was created, vessels were separated based on volume (small vessels in purple; large vessel in turquoise). (**F**) Filaments were created to calculate vessel length and number of branch points (red) and cells attached to vessels isolated and analyzed (blue).

RESULTS

Lectins Allow for Rapid Identification of Blood Vessels for 3D Surface Rendering

To rapidly identify all blood vessels in the brain, mice were injected via tail vein with *Lycopersicon esculentum* tomato lectin 488 (Fig. 1). Lectin uniformly and strongly binds to vessels of varying sizes throughout the brain which can be visualized along with cell nuclei counterstained with DAPI [Robertson et al., 2015]. To quantify vessel parameters in the hippocampal region of interest (Fig. 1) deconvoluted Z-stack are taken through a series steps involving unbiased image optimization, 3D surface rendering, background removal and lastly, volume, surface area, and filament tracing algorithms using the Imaris software suite (Fig. 2). This process was systematically

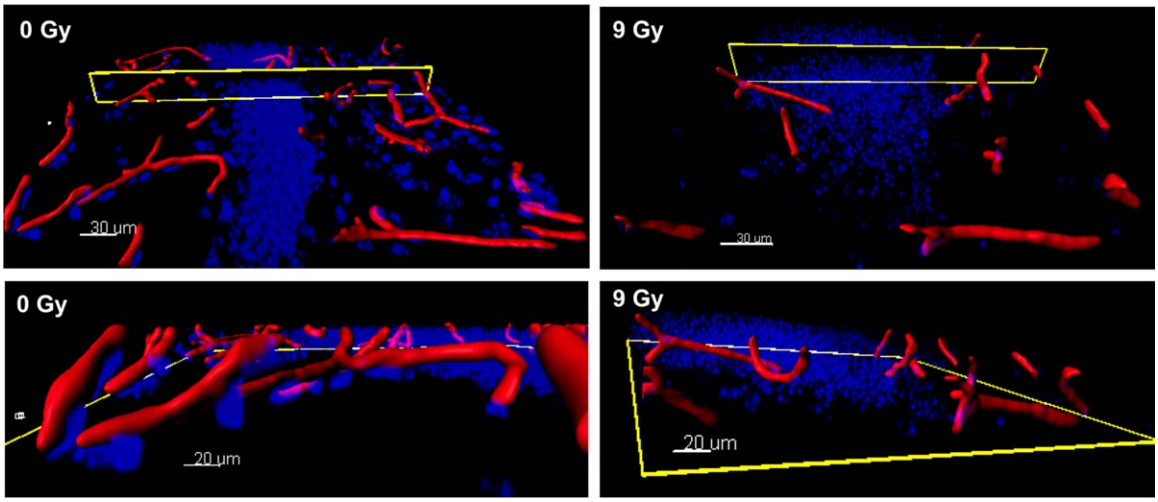

Fig. 4. Surface rendering allows for 3D analysis of microvessels. A reduction in microvessels was observed within the DG following 9 Gy irradiation compared to 0 Gy controls. Surfaces (red) were created from lectin-stained vessels and nuclei were DAPI counterstained (blue). Images were taken at 60×/1.4 NA. Scale bars = 30 µm (top) and 20 µm (bottom).

applied and provided for the high resolution analysis and 3D surface rendering of deconvoluted confocal z-stacks (Fig. 3A,B). Images were analyzed using a "Blend" setting to observe vessels in 3D (Fig. 3C) and background nuclei were removed from the analysis to create the 3D surfaces of vessels (Fig. 3D). Microvessels were analyzed seperately, where relatively smaller vessels were shown in purple and larger vessels were shown in turquoise (Figs. 3E and 3F). Individual cells comprising a vessel were identified using the DAPI channel to visualize nuclear staining along the 3D surface (Fig. 3F). Filament tracing was employed to quantify vessel length and branch points (shown in red, Fig. 3F). The uniformity of lectin staining throughout the hippocampus can also be presented in 3D, where surface rendering of microvessels provides a useful tool for visualizing and quantifying radiation-induced changes in microvessel volume (Fig. 4). These types of high resolution Z-stacks can also be merged and rotated about multple axes to create an animated rendering of fluorescent vessels. An example of this is provided in the Supporting Information (Movie S1).

Cranial Irradiation Reduced Microvessel Volume in the Dentate Gyrus

Mice were subjected to 9 Gy head-only x-irradiation and were admininstered *Lycopersicon esculentum* tomato lectin 594 via tail vein injection 2 days post-irradiation. Representative fluorescent images demonstrate a reduction in microvessel density/abundance in the irradiated hippocampus relative to 0 Gy controls (Figs. 5A and 5B). Surfaces were created using identical threshold parameters for both unirradiated and irradiated tissues to quantify microvessel volume, allowing for accurate volume quantification by normalizing fluorescent intensities in unirradiated and irradiated tissues (Figs. 5C and 5D). Average microvessel volumes were also normalized for variations in number of Z-stacks and area of tissues by calculating volume/μm^3. Quantification of the microvasculature in the hippocampus of unirradiated animals demonstrated a mean volume/μm^3 of 2247 ± 121 while volumes were significantly reduced in the hippocampus of irradiated mice with a mean volume/μm^3 of 1474 ± 98 ($P \leq 0.0001$, Fig. 5E).

Quantification of Multiple Vessel Parameters by 3D Surface Analysis

Mean area and total number of vessels were quantified for irradiated and control animals using 3D surface analysis. To quantify vessel length and number of branch points, a filament trace was created where threshold parameters remained identical for both control and irradiated tissues. Analyses of each experimental group within a normalized area show that all microvessel structural parameters are reduced in the irradiated animals compared to controls (Table I). With 0 Gy controls set to unity, relative differences in multiple microvessel parameters were measured in the 9 Gy irradiated animals. As shown in Figure 6, mean vessel volume/μm^3 in irradiated mice was significantly reduced to $65\% \pm 5\%$ relative to 0 Gy controls ($P \leq 0.001$). Similarly, the mean area of hippocampal microvessels in irradiated mice was significantly reduced to $76\% \pm 3\%$ relative to unirradiated controls ($P \leq 0.01$). Lastly, the number of branch points was significantly reduced in animals subjected to 9 Gy of irradiation with $57\% \pm 10\%$ relative to 0 Gy controls

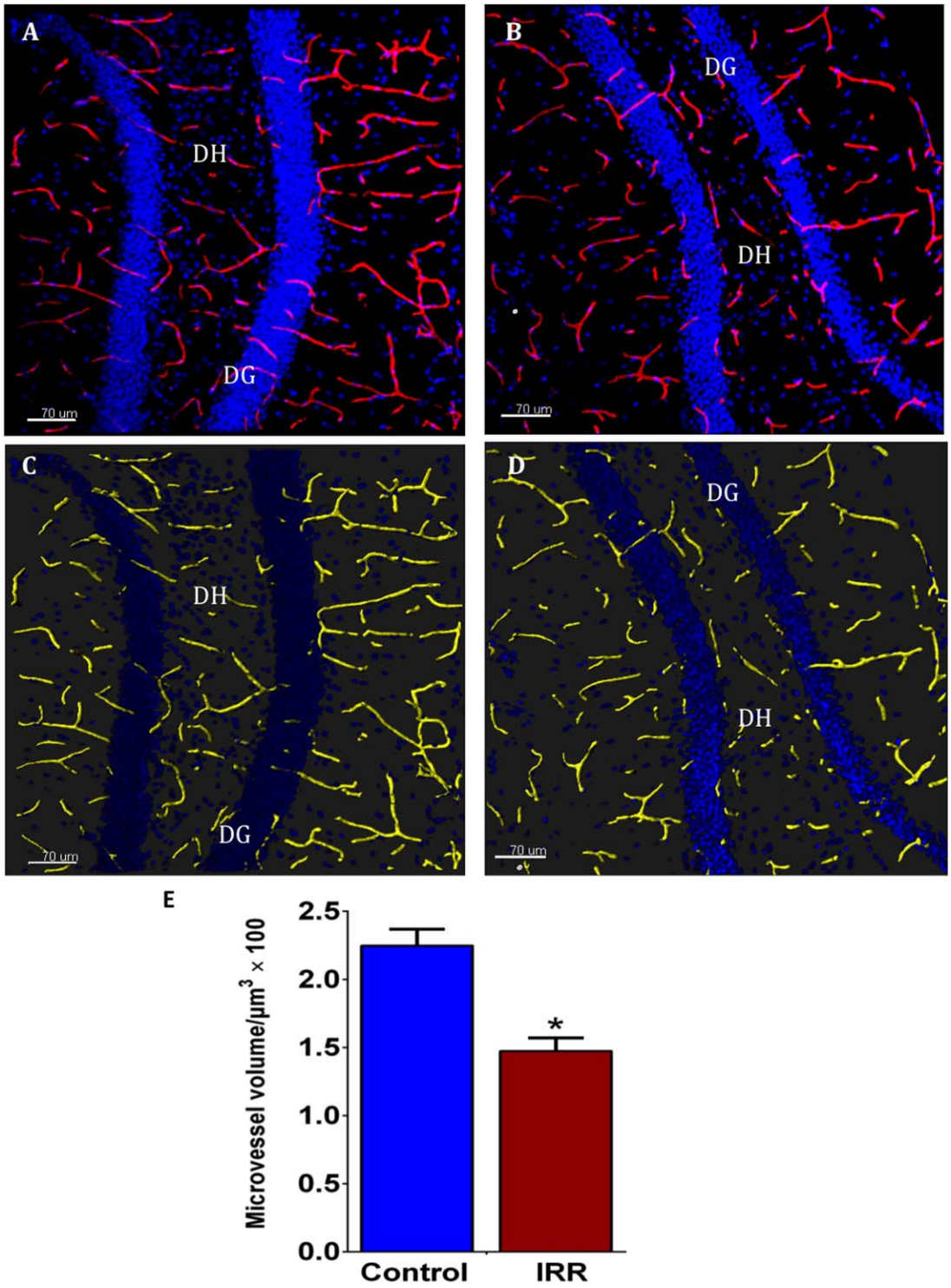

Fig. 5. Cranial irradiation reduces microvasculature volume in the mouse dentate gyrus. Representative fluorescent images of vessels labeled with tomato lectin-594 (red) in (**A**) 0 Gy and (**B**) 9 Gy tissues show reduced vasculature in the irradiated hippocampus compared to 0 Gy control. (**C,D**) Representative images of 3D surfaces (yellow) constructed over microvessels to normalize fluorescence intensities and quantify change in volume in 0 and 9 Gy tissues, respectively. (**E**) Quantification of microvessel volume/μm^3 in the mouse dentate hilus (DH) and dentate gyrus (DG) show significant reduction of vessel volume 2 days post-irradiation compared to unirradiated controls. Data are presented as mean ± SEM; four mice per group. * $P \leq 0.001$. Scale bar 70 μm. Nuclei counterstained with DAPI (blue).

TABLE I. Raw Microvessel Parameter Data From Control (0 Gy) and Irradiated (9 Gy) Mice

	0 Gy Mean	St. Dev.	9 Gy Mean	St. Dev.
Total volume (μm^3)	2.2×10^5	4.5×10^4	1.5×10^5	2.2×10^4
No. of branch points	30.6	9.5	16.1	5.8
Mean diameter (μm)	4.97	0.31	4.48	0.27
Surface area (μm^2)	1.5×10^5	1.9×10^4	1.1×10^5	1.5×10^4
Total length (μm)	5.7×10^3	8.3×10^2	4.7×10^3	6.2×10^2
Volume of tissue analyzed (μm^3)	9.4×10^6		9.4×10^6	

All parameters are reduced in irradiated animals compared to unirradiated controls. The volume of tissue analyzed was the same for both groups.

TABLE II. Comparison Between Imaris and Neurolucida

Parameters[a]	Imaris	Neurolucida
No. of sections analyzed/animal	~4	6
CNS volume analyzed/animal (μm^3)	3.7×10^7	4.3×10^7
Location of CNS analyzed	Dentate gyrus	Subgranular zone
Vessel diameter analysis	Yes	No
3D projection analysis	Yes	No
Automated surface rendering of vessels	Yes	No
Labor intensive	No	Yes

*Comparison between different analytical module shows that Imaris is superior to Neurolucida for quantification of microvessels in 3D. Imaris is capable of quantifying vessel diameter, as well as automated surface analysis, which results in more rapid analysis compared to Neurolucida.

($P \leq 0.05$, Fig. 6). The lower number of branch points correlated with the reduced length of remaining vessels. Although not statistically significant, total numbers and mean lengths of vessels were also reduced to 90% ± 3% and 87% ± 4%, respectively, in 9 Gy irradiated animals compared to unirradiated controls.

Cranial Irradiation Reduces RECA-1 + Microvessels in the Rat Hippocampus

To validate our methods and findings from the mouse studies and to determine the persistence of the observed effects of irradiation on microvessels in the hippocampus we also evaluated rats 1 month after cranial irradiation (10 Gy). In place of the lectin staining used in the mouse study, we used RECA-1 immunostaining to visualize vessels in the rat hippocampus. Microvessels stained positively for RECA-1 within the dentate gyrus were traced using Neurolucida to quantify volume/μm^3. This analysis revealed a marked difference in the number of RECA-1+ vessels in the irradiated hippocampus compared to unirradiated controls (Figs. 7A and 7B). Quantification of microvasculature density revaled a three-fold decrease in irradiated animals relative to unirradiated controls (Fig. 7C). These data demonstrate a greater magnitude, but qualitatively similar result in the rats over a longer post-irradiation interval (1 month) compared to the data obtained in mice after a shorter post-irradiation time (2 days).

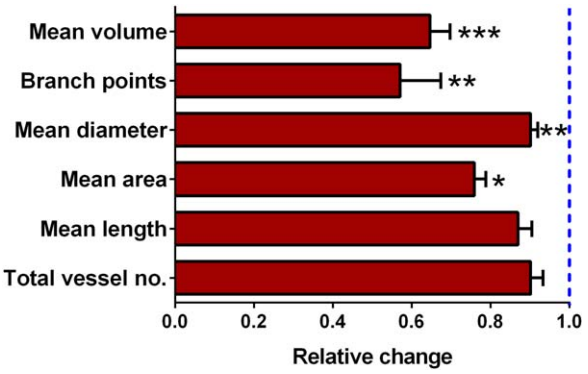

Fig. 6. Reduction in blood vessel parameters within the hippocampus of irradiated mice. All values were normalized to unirradiated controls (blue dashed line). Mean volume ($\mu m^2/\mu m^3 \times 100$), number of branch points, mean area (μm^2), mean length (μm) and total vessel number were all reduced 2 days following 9 Gy cranial irradiation relative to 0 Gy controls. Data are presented as the mean ± SEM, which were normalized against relative radiation-induced changes of each individual endpoint relative to the average control values; four mice per group. $*P = 0.05$, $**P = 0.01$, $***P = 0.001$; unpaired t test with Welch's correction.

DISCUSSION

The functional integrity of the vasculature dictates the health of nearly every normal tissue in the body. This is particularly true for the CNS where even modest disruption to the blood brain barrier (BBB) or cerebral blood flow can have dire short and long-tem consequences [Zlokovic 2008, 2010]. The vasculature is also susceptible to exogenous and endogenous insults, including the vast majority of the physical and chemical agents used to deter the spread of primary and metastatic cancer. Radio- and chemotherapies used to combat brain cancer have been shown to compromise cognition after the cessation of treatment [Butler et al., 2006; Myers, 2009], and represent a major concern in the therapeutic management of cancer [Vardy et al., 2008]. The causes of treatment-associated cognitive impairment are many, including increased neuroinflammation and disruptions to host neuronal structure [Parihar and Limoli, 2013; Parihar et al., 2014; Acharya et al., 2015a]. Given the high metabolic demands of the CNS [Simonian and Coyle, 1996; Smith et al., 1999] that are in large part dependent on cerebral blood flow, it is important to consider how changes in the vascular bed might contribute to neurocognitive outcomes following cancer treatments. For this reason, animals subjected to head-only irradiation were analyzed for vascular disruptions in the brain.

To address these issues, we implemented two relatively new and different strategies using two distinct rodent models in order to quantitatively analyze radiation-induced microvascular changes in the brain. To assess acute changes

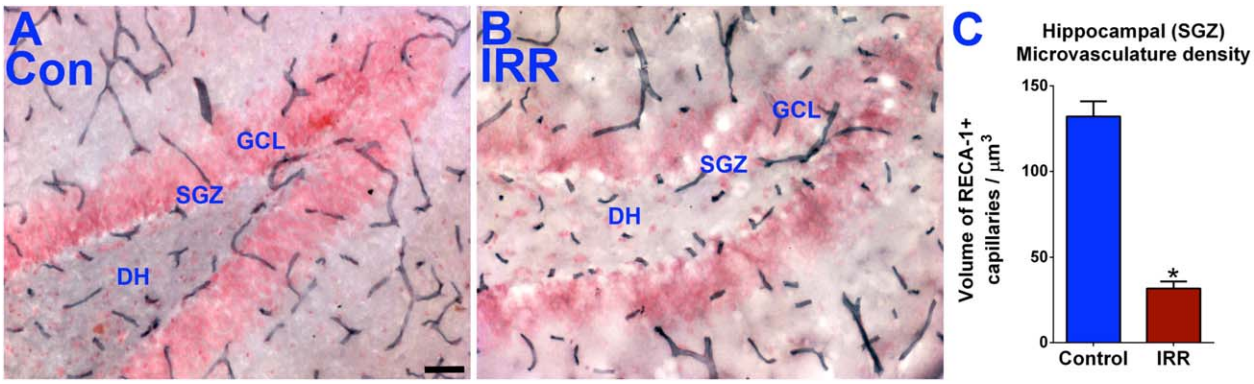

Fig. 7. Cranial irradiation also affects hippocampal microvasculature in rat brain 1 month post-irradiation. (**A**,**B**) Quantitative analysis of RECA-1^{+} immunoreactive capillaries showed marked reductions in capillary distribution and shrinkage 1 month following head-only irradiation (black with nuclear fast red counterstain; dentate hilus (DH), subgranular zone (SGZ) and granule cell layer (GCL); Scale bar 50 µm). Neurolucida assessment of capillary volume within the hippocampal SGZ showed a significant reduction in capillary volume post-irradiation (**C**). Data are presented as mean ± SEM; four to six rats per group. *$P < 0.002$. Scale bar 50 µm.

in the microvasculature, mice were subjected to intravascular injection with a fluorescently tagged lectin 2 days after cranial irradiation [Robertson et al., 2015]. Confocal analysis confirmed the specificity of vascular labeling and provided the Z-stacks necessary for 3D deconvolution and rendering of vasculature surface area and volume (Figs. 3–5). Quantification of microvessel volume in the irradiated hippocampus revealed significant reductions in capillary density compared to unirradiated controls (Fig. 5). Similar analyses performed to calculate additional structural parameters of vessels including branch points, area, length, and number confirmed the capability of irradiation to reduce nearly every endpoint analyzed, albeit not all significantly (Fig. 6). Past studies have confirmed the capability of irradiation to compromise the vascular bed, including changes in vessel wall thickness, dilation and endothelial apoptosis [Reinhold et al., 1990]. Early apoptosis (<24 h) leads to relatively modest reductions in endothelial cell numbers and typically occur at doses in excess of those used in this study [Ljubimova et al., 1991]. Radiation-induced endothelial cell apoptosis is largely dependent on the second messenger ceramide, generated by the activity of acid sphigomylinases [Pena et al., 2000; Li et al., 2003]. While breakdown of the BBB is largely attributed to vascular apoptosis and disruption of tight junctions [Li et al., 2003; Yuan et al., 2003], the lower doses used here did not lead to any overt leakage of the labeled lectin into the brain parenchyma, suggesting the absence of any significant acute changes in vascular permeability. Despite this, our data demonstrate that some of the early acute effects of cranial irradiation include significant disruption to the structure and density of microvessels in the brain.

While acute effects can be problematic to CNS function, the most critical normal tissue complications such as white matter necrosis and cognitive impairment that are associated with radiotherapy of the brain transpire at delayed times [Tofilon and Fike, 2000; Fike et al., 2009]. These so-called late effects are temporally coincident with the onset and progression of neurocognitive sequelae, and are generally not dependent on the early changes measured after irradiation [Tofilon and Fike, 2000; Fike et al., 2009]. To ascertain whether head-only irradiation caused longer-term changes in the vasculature of the brain, rats were analyzed for alterations in capillary density 1 month after exposure. Immunostaining for RECA-1+ capillaries revealed qualitative differences in vessel distribution, length and density in the dentate gyrus of the hippocampus (Fig. 7). Quantification of these morphological changes showed that irradiation caused a persistent and significant reduction in the density of hippocampal microvessels. These data demonstrate longer-term effects of irradiation on the vascular bed, and suggest that radiation-induced disruption of the microvascular could compromise cerebral blood flow and interfere with neurotransmission and cognitive function.

Present results demonstrate the utility of two distinct approaches for quantifying radiation-induced microvascular changes in the brain of cranially exposed mice and rats. Each strategy utilizes software alogorithms able to quantify surface area and volume of lectin- or immuno-stained capillaries. Comparison of the two software platforms indicates that Imaris is superior to Neurolucida for a rapid quantification of microvessel parameters in 3D (Table II). The capability of Imaris to automate surface analysis, including 3D rendering, provides distinct time saving advantages compared to Neurolucida (Table II). However, both these quantitative tools provide the capability to undertake detailed structural analyses of the vasculature. Here we showed that head-only irradiation resulted in short and longer-term reductions in capillary density in mice and rats, respectively. Our selection of models was designed to illustrate how different techniques could be applied to the study of radiation effects on the vasculature of clearly different rodent models. While it was not our intent to compare these models directly, caution must be exercised when

interpreting these data sets, as the temporal responses between mice and rats may differ over acute and more chronic post-irradiation times. Doses were selected to match past studies used to elicit cognitive decline in rodents [Acharya et al., 2011, 2015b], but remain significantly lower than those used for curative cranial radiotherapy [Butler et al., 2006]. Doses used in our work also avoid overt tissue injury, as past preclinical and clinical studies have indicated that neurocognitive sequelae will likely occur far below the dose thresholds necessary for macroscopic tissue destruction [Tofilon and Fike, 2000; Fike et al., 2009]. The fact that 9–10 Gy caused acute and longer-term changes in mice and rats respectively, suggests that each of these labeling methodologies would be useful for elucidating more detailed dose and temporal responses of vascular damage in the brain. Precisely how these changes contribute to the many neurocognitive side effect of cranial irradiation remains uncertain, but data indicate that disruptions to the microvasculature may contribute to the perturbation of neurotransmission and cognitive function.

AUTHOR CONTRIBUTIONS

CLL and MMA designed and conceived the studies. BMC, BDA, SNB, and NWH collected the data. MMA and BMC analyzed the data and prepared figures. BMC, JEB, and CLL prepared the manuscript. All authors approved the final manuscript.

ACKNOWLEDGMENTS

We would like to thank Dr. Richard T. Robertson at UC Irvine for his help showing us the lectin methodology.

REFERENCES

Abayomi OK. 1996. Pathogenesis of irradiation-induced cognitive dysfunction. Acta Oncol 35:659–663.

Acharya MM, Christie LA, Lan ML, Giedzinski E, Fike JR, Rosi S, Limoli CL. 2011. Human neural stem cell transplantation ameliorates radiation-induced cognitive dysfunction. Cancer Res 71: 4834–4845.

Acharya MM, Martirosian V, Chmielewski NN, Hanna N, Tran KK, Liao AC, Christie LA, Parihar VK, Limoli CL. 2015a. Stem cell transplantation reverses chemotherapy-induced cognitive dysfunction. Cancer Res 75:676–686.

Acharya MM, Martirosian V, Christie LA, Riparip L, Strnadel J, Parihar VK, Limoli CL. 2015b. Defining the optimal window for cranial transplantation of human induced pluripotent stem cell-derived cells to ameliorate radiation-induced cognitive impairment. Stem Cells Transl Med 4:74–83.

Butler JM, Rapp SR, Shaw EG. 2006. Managing the cognitive effects of brain tumor radiation therapy. Curr Treat Options Oncol 7:517–523.

Fike JR, Rosi S, Limoli CL. 2009. Neural precursor cells and central nervous system radiation sensitivity. Semin Radiat Oncol 19: 122–132.

Greene-Schloesser D, Robbins ME, Peiffer AM, Shaw EG, Wheeler KT, Chan MD. 2012. Radiation-induced brain injury: A review. Front Oncol 2:73.

Li YQ, Chen P, Haimovitz-Friedman A, Reilly RM, Wong CS. 2003. Endothelial apoptosis initiates acute blood-brain barrier disruption after ionizing radiation. Cancer Res 63:5950–5956.

Ljubimova NV, Levitman MK, Plotnikova ED, Eidus L. 1991. Endothelial cell population dynamics in rat brain after local irradiation. Br J Radiol 64:934–940.

McBride WH. 1995. Cytokine cascades in late normal tissue radiation responses. Int J Radiat Oncol Biol Phys 33:233–234.

Meyers CA. 2000. Neurocognitive dysfunction in cancer patients. Oncology (Williston Park) 14:75–79; discussion 79, 81-72, 85.

Mizumatsu S, Monje M, Morhardt D, Rola R, Palmer T, Fike J. 2003. Extreme sensitivity of adult neurogenesis to low doses of X-irradiation. Cancer Res 63:4021–4027.

Myers JS. 2009. Chemotherapy-related cognitive impairment. Clin J Oncol Nurs 13:413–421.

Parihar VK, Limoli CL. 2013. Cranial irradiation compromises neuronal architecture in the hippocampus. Proc Natl Acad Sci USA 110: 12822–12827.

Parihar VK, Acharya MM, Roa DE, Bosch O, Christie LA, Limoli CL. 2014. Defining functional changes in the brain caused by targeted stereotaxic radiosurgery. Transl Cancer Res 3:124–137.

Parihar VK, Pasha J, Tran KK, Craver BM, Acharya MM, Limoli CL. 2015. Persistent changes in neuronal structure and synaptic plasticity caused by proton irradiation. Brain Struct Funct 220: 1161–1171.

Pena LA, Fuks Z, Kolesnick RN. 2000. Radiation-induced apoptosis of endothelial cells in the murine central nervous system: Protection by fibroblast growth factor and sphingomyelinase deficiency. Cancer Res 60:321–327.

Reinhold HS, Calvo W, Hopewell JW, van der Berg AP. 1990. Development of blood vessel-related radiation damage in the fimbria of the central nervous system. Int J Radiat Oncol Biol Phys 18: 37–42.

Robertson RT, Levine ST, Haynes SM, Gutierrez P, Baratta JL, Tan Z, Longmuir KJ. 2015. Use of labeled tomato lectin for imaging vasculature structures. Histochem Cell Biol 143:225–234.

Simonian NA, Coyle JT. 1996. Oxidative stress in neurodegenerative diseases. Annu Rev Pharmacol Toxicol 36:83–106.

Smith KJ, Kapoor R, Felts PA. 1999. Demyelination: The role of reactive oxygen and nitrogen species. Brain Pathol 9:69–92.

Surma-aho O, Niemela M, Vilkki J, Kouri M, Brander A, Salonen O, Paetau A, Kallio M, Pyykkonen J, Jaaskelainen J. 2001. Adverse long-term effects of brain radiotherapy in adult low-grade glioma patients. Neurology 56:1285–1290.

Tofilon PJ, Fike JR. 2000. The radioresponse of the central nervous system: A dynamic process. Radiat Res 153:357–370.

van der Kogel AJ. 1986. Radiation-induced damage in the central nervous system: An interpretation of target cell responses. Br J Cancer Suppl 7:207–217.

Vardy J, Wefel JS, Ahles T, Tannock IF, Schagen SB. 2008. Cancer and cancer-therapy related cognitive dysfunction: An international perspective from the Venice cognitive workshop. Ann Oncol 19: 623–629.

Wong CS, Van der Kogel AJ. 2004. Mechanisms of radiation injury to the central nervous system: Implications for neuroprotection. Mol Interv 4:273–284.

Yuan H, Gaber MW, McColgan T, Naimark MD, Kiani MF, Merchant TE. 2003. Radiation-induced permeability and leukocyte adhesion in the rat blood-brain barrier: Modulation with anti-ICAM-1 antibodies. Brain Res 969:59–69.

Zlokovic BV. 2008. The blood-brain barrier in health and chronic neurodegenerative disorders. Neuron 57:178–201.

Zlokovic BV. 2010. Neurodegeneration and the neurovascular unit. Nat Med 16:1370–1371.